Monolayer-Precision Synthesis of Molybdenum Sulfide Nanoparticles and Their Nanoscale Size Effects in the Hydrogen Evolution Reaction

Bora Seo,[†,∥] Gwan Yeong Jung,[‡,∥] Young Jin Sa,[†] Hu Young Jeong,[§] Jae Yeong Cheon,[†] Jeong Hyeon Lee,[‡] Ho Young Kim,[‡] Jin Chul Kim,[‡] Hyeon Suk Shin,[†] Sang Kyu Kwak,[*,‡] and Sang Hoon Joo[*,†,‡]

[†]Department of Chemistry, [‡]School of Energy and Chemical Engineering, and [§]UNIST Central Research Facilities (UCRF), Ulsan National Institute of Science and Technology (UNIST), 50 UNIST-gil, Ulsan 689-798, Republic of Korea. [∥]These authors contributed equally.

ABSTRACT Metal sulfide-based nanostructured materials have emerged as promising catalysts for hydrogen evolution reaction (HER), and significant progress has been achieved in enhancing their activity and durability for the HER. The understanding of nanoscale size-dependent catalytic activities can suggest critical information regarding catalytic reactivity, providing the scientific basis for the design of advanced catalysts. However, nanoscale size effects in metal sulfide-based HER catalysts have not yet been established fully, due to the synthetic difficulty in precisely size-controlled metal sulfide nanoparticles. Here we report the preparation of molybdenum sulfide (MoS_2) nanoparticles with monolayer precision from one to four layers with the nearly constant basal plane size of 5 nm, and their size-dependent catalytic activity in the HER. Using density functional theory (DFT) calculations, we identified the most favorable single-, double-, and triple-layer MoS_2 model structures for the HER, and calculated elementary step energetics of the HER over these three model structures. Combining HER activity measurements and the DFT calculation results, we establish that the turnover frequency of MoS_2 nanoparticles in the HER increases in a quasi-linear manner with decreased layer numbers. Cobalt-promoted MoS_2 nanoparticles also exhibited similar HER activity trend. We attribute the higher HER activity of smaller metal sulfide nanoparticles to the higher degree of oxidation, higher Mo—S coordination number, formation of the 1T phase, and lower activation energy required to overcome transition state. This insight into the nanoscale size-dependent HER activity trend will facilitate the design of advanced HER catalysts as well as other hydrotreating catalysts.

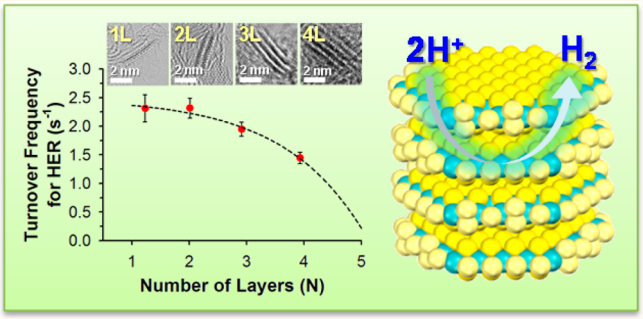

KEYWORDS: MoS_2 · monolayer-precision synthesis · nanoscale size effect · catalyst · hydrogen evolution reaction

Metal sulfide nanostructures represent a novel class of 2-dimensional (2D) materials, and constitute a topic of tremendous current interest.[1−3] Burgeoning research regarding metal sulfide nanostructures primarily stems from their intriguing physicochemical properties such as tunable electronic and optical characteristics as well as their broad applicability as transistors, topological insulators, batteries, and catalysts.[1−5] Notably, metal sulfide nanostructures have received rejuvenated attention as catalysts, particularly in the hydrogen evolution reaction (HER), which serves as a key reaction in renewable energy technologies.[4,6−10] Interest in metal sulfide-based HER catalysts has been inspired by theoretical calculations that predicted promising HER activity with MoS_2 nanostructures,[11,12] as well as experimental demonstrations based on the nanocrystallite[13] and molecular[14] model catalysts. In addition, the low cost and abundance of transition metal-based sulfides have prompted their potential use as replacements of state-of-the-art Pt-based HER catalysts. Recent efforts involving metal sulfide-based catalysts have primarily focused on enhanced HER activity and durability in an effort to narrow the performance gap between them and Pt-based catalysts. Strategies include the hybridization of metal sulfides with conducting carbon nanostructures,[15−20] use of amorphous phase metal sulfides,[9,21−25] addition of secondary metal,[26−30] engineering of active

* Address correspondence to shjoo@unist.ac.kr, skkwak@unist.ac.kr.

Received for review November 6, 2014 and accepted March 20, 2015.

Published online March 20, 2015
10.1021/acsnano.5b00786

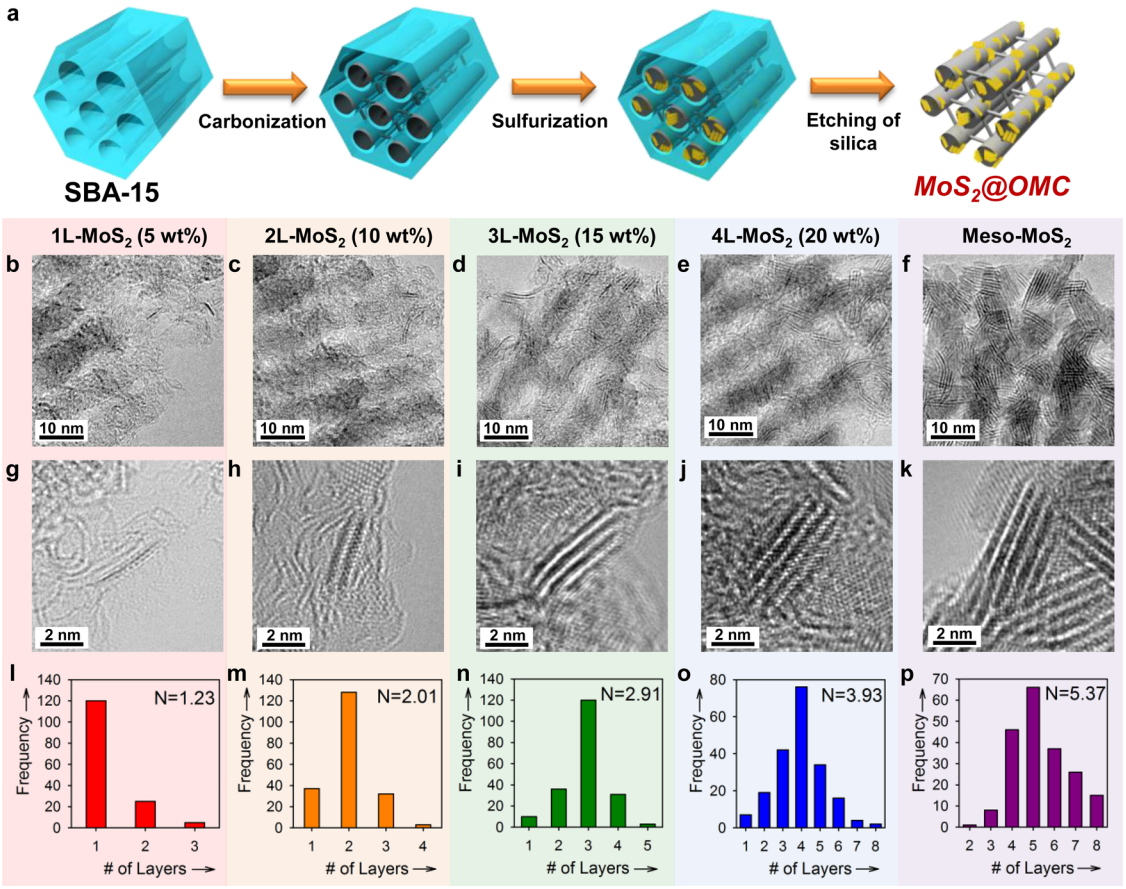

Figure 1. Synthesis and TEM characterization of MoS_2@OMC. (a) Synthetic scheme for MoS_2@OMC preparation. The inner pores of mesoporous silica template (SBA-15) were partially filled with carbon, followed by the growth of the MoS_2 nanoparticles in the residual pore space, and removal of SBA-15 template to produce the MoS_2@OMC nanostructure. SBA-15, sky blue; carbon, black; MoS_2 nanoparticles, yellow. (b–f) TEM images of (b) 1L-MoS_2@OMC, (c) 2L-MoS_2@OMC, (d) 3L-MoS_2@OMC, (e) 4L-MoS_2@OMC, and (f) Meso-MoS_2. Corresponding atomic resolution TEM images (g–k) and histograms for layer number distribution (l–p). The average number of MoS_2 layers is denoted as 'N' in (l–p).

edge sites or interlayer distances,[31−36] and the formation of 1T layer structured metal sulfides.[37−40]

The understanding of particle size effects, which probe trends in catalytic activity per surface site within a series of catalysts of varying particle sizes, can provide critical insights into catalytic reactivity.[41−43] In particular, studies utilizing catalysts below 5 nm, where the structural and electronic properties of nanoparticles exhibit the most drastic changes, can suggest compelling evidence. Hence, particle size effects have been a topic of keen interests during the last several decades, which have consequently led to the identification of molecular factors responsible for reactivity trends as well as a scientific basis for the design of advanced catalysts. In many benchmark catalytic reactions, such as CO oxidation and oxygen reduction reaction, size effects have been well established.[44−48] However, the nanoscale particle size effect for the HER by metal sulfide-based catalysts is not well established yet. The lack of such studies stems primarily from the difficulty in controlling the size of metal sulfide structures on the nanometer scale in the basal and edge plane directions; the anisotropic nature of layered MoS_2 dictates the energetically favorable horizontal growth, thus resulting in sheet or film-like structures.

In this work, we report the preparation of size-controlled MoS_2 nanoparticles with monolayer precision, and their size-dependent HER activity trends. We prepared MoS_2 nanoparticles embedded in ordered mesoporous carbon (MoS_2@OMC) nanostructures using mesoporous silica as a template (Figure 1a). In this design, the layer number of the MoS_2 nanoparticles could be controlled precisely from one to four layers in a layer-by-layer manner by varying the MoS_2 loading, while the basal plane size was maintained below 5 nm. On the basis of density functional theory (DFT) calculations, the most favorable structures of single-, double-, and triple-layer MoS_2 for the HER were identified, and the elementary step energetics of the HER over these MoS_2 structures was calculated. The size-controlled MoS_2@OMC nanostructures exhibited high activity in the HER, and they provided an unprecedented insight into the increasing HER activity with decreasing MoS_2 layer numbers in a quasi-linear manner. A similar reactivity trend was also found with cobalt-doped $CoMoS_2$@OMC nanostructures.

The higher HER activity of smaller metal sulfide nanoparticles was attributed to the collective contribution of the higher degree of oxidation, higher Mo−S coordination number, formation of the 1T phase, and lower activation energy required to overcome transition state.

RESULTS AND DISCUSSION

Preparation and Characterization of MoS_2@OMCs with Controlled MoS_2 Layer Number. Figure 1a shows a schematic of the preparation of the MoS_2@OMC nanostructures. The first step involved the partial filling of the pores of the SBA-15 mesoporous silica template with carbon structures, which was carried out *via* a similar method to that used in the CMK-3 mesoporous carbon synthesis,[49] except for the decreased amount of the carbon source. Subsequently, the molybdenum precursor was impregnated in the silica−carbon composite, followed by drying and sulfidation using H_2S gas. The etching of silica from the silica−carbon-MoS_2 ternary composite afforded the MoS_2@OMC nanostructures. On the basis of previous reports on the preparation of mesoporous MoS_2 (Meso-MoS_2),[50,51] the sulfidation temperature was set at 600 °C for the preparation of MoS_2@OMC nanostructures. The detailed synthetic procedure for the MoS_2@OMCs is described in Materials and Methods section. The nominal content of MoS_2 was controlled from 5 to 20 wt %, and inductively coupled plasma optical emission spectrometry (ICP-OES) analysis indicated successful incorporation of the desired amount of the MoS_2 nanoparticles (Supporting Information Table S1).

Scanning electron microscope (SEM) images of the MoS_2@OMC nanostructures (Supporting Information Figure S1b,e) revealed that the short rod-like morphology of the SBA-15 template (Figure S1a) was nearly preserved in the templated replicas. Energy dispersive spectroscopy (EDS) elemental mapping images (Supporting Information Figure S2) confirmed the successful incorporation of the respective elements (Mo, S, and C) in the MoS_2@OMCs. Transmission electron microscope (TEM) images of the MoS_2@OMCs (Figure 1b−e and Supporting Information Figure S3a−d) showed that the MoS_2 nanoparticles were successfully embedded and uniformly distributed within the carbon nanorod arrays. From the TEM images, it was evident that the layer number (or edge plane size) of the MoS_2 nanoparticles increased with increasing MoS_2 content, while the basal plane size was maintained below 5 nm regardless of MoS_2 loading (Supporting Information Table S2). Significantly, atomic resolution TEM (AR-TEM) image (Figure 1g) and layer number distribution (Figure 1l) established that the lowest MoS_2 loading (5 wt %) sample was composed of nearly single layer MoS_2 nanoparticles (the calculated average layer number was 1.2). The AR-TEM image of this material (Figure 1g) clearly showed individual Mo and S atoms in single-layer MoS_2. The increase in the MoS_2 content to 10, 15, and 20 wt % in the MoS_2@OMC nanostructures led to layer number growth while preserving the basal plane size, leading to the formation of 2.0, 2.9, and 3.9 layer MoS_2 nanoparticles (Figure 1h−j for AR-TEM images and Figure 1m−o for layer number distributions). Hereafter, these materials are denoted as 1L-, 2L-, 3L-, and 4L-MoS_2@OMCs according to the MoS_2 layer number. From the TEM observations, it was found that at the initial stage, MoS_2 growth preferentially occurred in the thermodynamically favorable basal plane direction, which was limited by the confined nanopore space of the silica−carbon composite; with increased MoS_2 loading, the crystal growth took place *via* the layer-by-layer vertical stacking of MoS_2 layers, leading to a gradual increase in the layer number. The average crystallite size of the basal and edge planes in MoS_2 nanoparticles and their layer numbers, determined using TEM images, are summarized in Supporting Information Table S2. Notably, from the AR-TEM images of the MoS_2@OMC nanostructures (Figure 1h−j), the interlayer spacing of the (002) planes of MoS_2 was 0.64 nm, which was slightly larger than that of bulk MoS_2 (0.61 nm).[52] The enlarged spacing could originate from the curvatures and distortions of the (002) planes during the confined growth of the MoS_2 nanoparticles within the limited pore space of silica−carbon composite. In addition, the characterization of Meso-MoS_2 (Figure 1f,k,p; see Supporting Information for the details of its preparation) revealed that it was composed of 5.4 layer nanoparticles. Overall, we demonstrated the preparation of discrete size MoS_2 nanoparticles with monolayer precision, which featured a high percentage of catalytically active edge sites and a distorted (002) plane.

The MoS_2@OMC nanostructures were further characterized by X-ray diffraction (XRD) and nitrogen adsorption analysis. The high-angle XRD patterns of the MoS_2@OMCs (Figure 2a) were commensurate with that of the hexagonal MoS_2 standard (JCPDS card no: 75-1539). The edge plane direction (002) diffraction peak at 2θ = 14.1° became sharper with increased layer numbers in the edge plane. It is noteworthy that 1L- and 2L-MoS_2@OMCs exhibited featureless (002) diffraction peaks, which was in good agreement with the TEM observations. The small-angle XRD patterns of the MoS_2@OMCs (Supporting Information Figure S4) exhibited distinct X-ray diffraction lines below 2°, indicating a periodic mesostructure. The porous structure of the MoS_2@OMCs, as analyzed by nitrogen adsorption−desorption isotherms (Supporting Information Figure S5 and S6), indicated uniform mesopores, large Brunauer−Emmett−Teller (BET) surface areas (as high as 1090 $m^2\ g^{-1}$), and large pore volumes (Supporting Information Table S3). As expected, the increase in the MoS_2 content in MoS_2@OMCs resulted in a decreased BET surface area and pore volume.

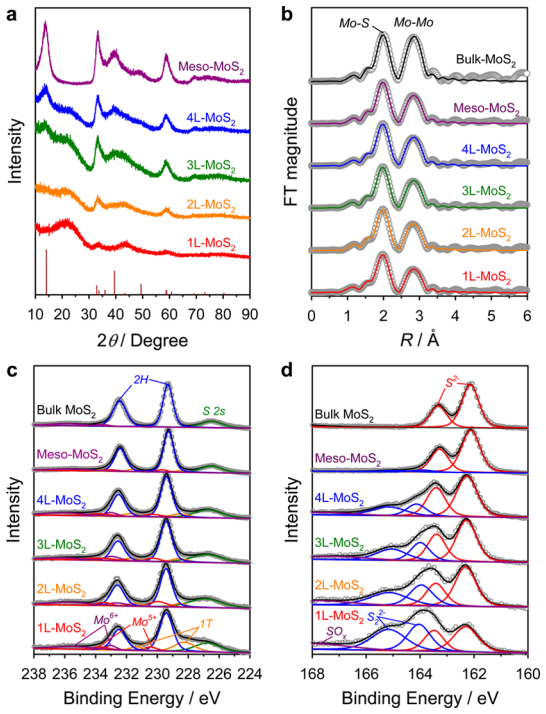

Figure 2. Structural and electronic characterization. (a) Wide-angle XRD patterns, with reference pattern for 2H MoS_2 crystal structure (Joint Commission for Powder Diffraction Standard (JCPDS): #75-1539) displayed as vertical bars. (b) Mo K-edge EXAFS fitting spectra. Detailed fitting parameters are summarized in Supporting Information Table S4. (c and d) XPS spectra of (c) Mo 3d and S 2s and (d) S 2p orbitals of the samples.

The local coordination environment of MoS_2 in MoS_2@OMCs was investigated by extended X-ray absorption fine structure (EXAFS). The Fourier transformed k^3-weighted Mo K-edge EXAFS spectra (Figure 2b and Supporting Information Table S4) exhibited two main peaks at 1.96 and 2.81 Å, which correspond to Mo−S and Mo−Mo bonds, respectively. With decreased layer numbers in MoS_2, the relative peak intensity for Mo−Mo bonding compared to that of Mo−S bonding decreased and the coordination number (CN) ratio between Mo−S and Mo−Mo (N_s/N_{Mo}) increased (Supporting Information Figure S7). The electronic structures of the samples were accessed with X-ray photoelectron spectroscopy (XPS) analysis (Figure 2c,d). In the Mo 3d XPS spectra (Figure 2c), the peaks at 229.3−229.4 eV (Mo $3d_{5/2}$) and 232.4−233.0 eV (Mo $3d_{3/2}$) (shown in blue) were predominantly observed, which can be matched with the oxidation state of Mo^{4+}. The two doublets at higher binding energies, corresponding to Mo^{5+} (red) and Mo^{6+} (purple) oxidation states were observed. The oxide species appear to be generated during HF etching of silica and subsequent exposure to air.[31] The gentle oxidation is known to be advantageous for HER catalysis by formation of pits which expose more edge sites.[52] The oxide peaks gradually developed with decreased MoS_2 layer number, presumably due to the propensity of Mo toward surface oxidation in smaller MoS_2 nanoparticles. Notably, the increase in the intensity of the doublet peaks around 228.3 and 231.4 eV from the bulk MoS_2 to 1L-MoS_2@OMC nanostructure suggested the evolution of structurally distorted 1T phase MoS_2 with decreasing layer number.[39,40] In the deconvoluted spectra of the S 2p region (Figure 2d), the bulk MoS_2 and Meso-MoS_2 samples showed main peaks at 162.1−162.3 eV (S $2p_{3/2}$) and 163.3−163.5 eV (S $2p_{1/2}$) that correspond to the S^{2-} species.[21] For the MoS_2@OMC nanostructures, the peaks for S_2^{2-} ligands at higher binding energies (163.9−164.1 eV and 164.9−165.2 eV for S $2p_{3/2}$ and S $2p_{1/2}$, respectively) gradually evolved with decreasing MoS_2 layer numbers at the expense of S^{2-} species. The gradual increase of the unsaturated S_2^{2-} peak together with a decrease in the number of layers may indicate an increasing number of bridging and terminal S_2^{2-} ligands which are known to correlate with active sites and defect, respectively.[35,53] Moreover, 1L-MoS_2@OMC exhibited a peak corresponding to sulfuric oxide (SO_x) species, indicative of the most enhanced oxidation state among the MoS_2@OMC nanostructures. Overall, EXAFS and XPS suggested the increased coordination of Mo−S bonding, increased presence of S_2^{2-} ligands, and enhanced surface oxidation with decreased layer numbers in MoS_2 nanoparticles.

Gibbs Free Energies of Hydrogen Adsorption on MoS_2 Structures. We theoretically explored the Gibbs free energy of the adsorbed hydrogen on MoS_2 structures in vacuum condition by DFT calculations. This calculation was designed to estimate appropriate coverage of sulfur on Mo- and S-edges. Significantly, we investigated single- and double-layer MoS_2,[12,54] as well as previously unexplored triple-layer MoS_2 structures, thereby providing an unprecedented level of insights into the energetics of hydrogen adsorption on MoS_2. Figure 3a shows the structural models for Mo(10$\bar{1}$0) and S($\bar{1}$010) edges with varying sulfur coverage. Models A and A′ represent Mo-edge structures covered with 50% and 100% S atoms, respectively, whereas Models B and B′ correspond to S-edge structures with 75% and 100% S atoms, respectively. Figure 3b shows the representative slab models for single-, double-, and triple-layer (denoted as 1L, 2L, and 3L, respectively) MoS_2, and Supporting Information Figure S8 displays all the model structures of interest and sulfur sites for a stable adsorption of hydrogen atoms. We found Model B′, which is a more stable form than those used in previous studies (Supporting Information Figure S9).[55−57] The values of Gibbs free energy (ΔG^0_H), which were obtained through calculating the binding energy of hydrogen (ΔE_H), are presented in Supporting Information Table S5. We point out that, for more accurate calculations of ΔG^0_H, the temperature effect was included (Supporting Information). A Gibbs free energy near zero suggests superior HER activity.[11]

The ΔG^0_H with 1L MoS_2 models (Figure 3c) was first calculated. It was revealed that, for Mo- and S-edge

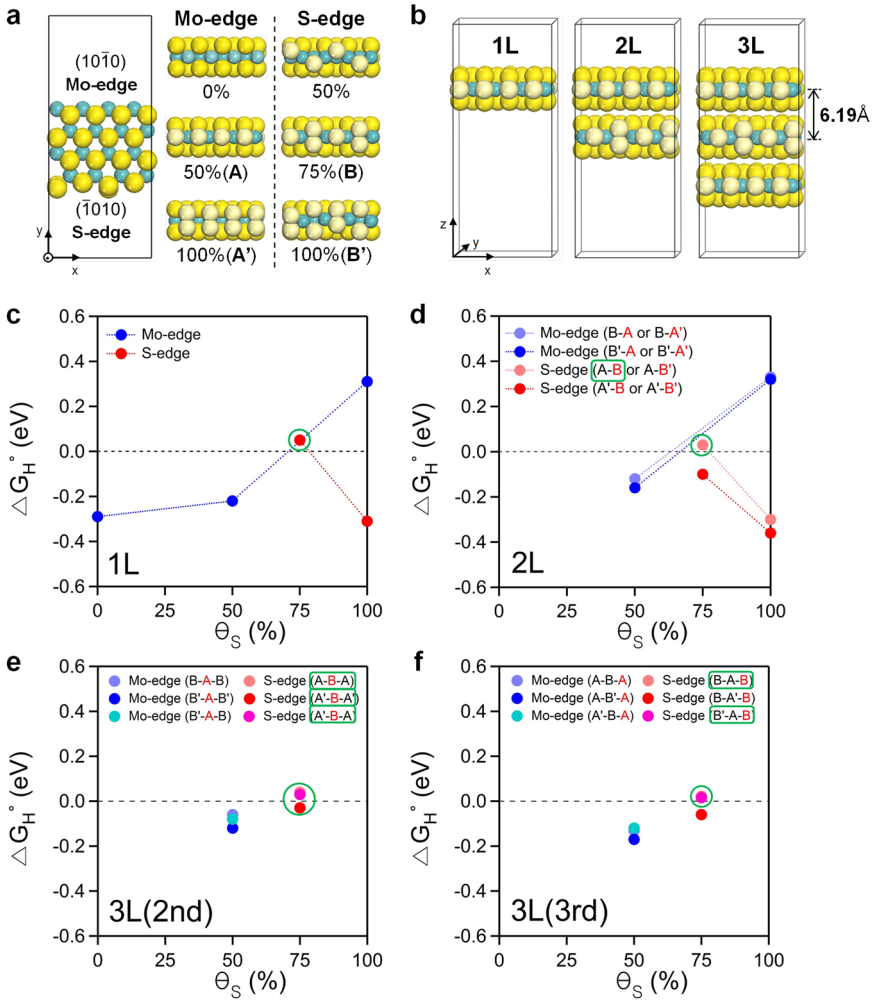

Figure 3. DFT calculations of the Gibbs free energy for H adsorption on the MoS_2 structures. (a) Top and side views of the semi-infinite slab models of Mo- and S-edge sites in MoS_2 with different degree of sulfur coverage. The S atoms along the edge and at terrace sites are represented by light and dark yellow spheres, respectively, and Mo atoms are presented as blue-green spheres. A supercell structure (*i.e.* *x*:12.84 Å, *y*:30.0 Å, *z*:30.0 Å) was created by four Mo atoms in the *x*, *y* directions. The slab model is only periodic in the *x* direction, and the Mo- and S-edges are exposed in the *y* direction. The terms, A, A′, B, and B′ represent Mo-edge (50% S), Mo-edge (100% S), S-edge (75% S), and S-edge (100% S) structures, respectively (Supporting Information Figure S8). (b) Representative layer models for 1L, 2L, and 3L MoS_2. The slab models for 2L and 3L are stacked with a layer center-to-center distance of 6.19 Å, and a vacuum space is introduced above and below the layer models. (c–f) The Gibbs free energy (ΔG^0_H) for hydrogen adsorption on the (c) 1L, (d) 2L, (e) 3L (2nd), and (f) 3L (3rd) MoS_2 models with varying degree of sulfur coverage (θ_S). The '2nd' and '3rd' indicate that hydrogen adsorption occurs at the 2nd layer and 3rd layer (equivalent to the 1st layer) in the 3L models, respectively. The green boxes in the legends and green circles in the plots correspond with each other and represent the most suitable points for the HER. The red letters in the legends indicate the location of the layers at which hydrogen adsorption occurs.

structures, Models A (50% S) and B (75% S) are favorable structures for the HER, respectively. In the calculation of ΔG^0_H with the 2L MoS_2 models (Figure 3d), the bond stability was affected by the sulfur coverage of the H-adsorbed layer as well as the edge configurations of adjacent layers on the same side. The Mo-edge(0% S) was not used to construct the 2L models, since the Mo-edge(0% S) has been known to be unstable and the adsorbed hydrogen on this layer shows strong adsorption, which consequently indicates difficult desorption (see Materials and Methods section).[58] By considering the inclusion of assorted energies induced from the temperature effect, the ΔG^0_H of Model A-B where hydrogen adsorbed on the B layer was found to be the most suitable structure for the HER.

Next, DFT calculations were extended to the 3L MoS_2 models which were constructed based on the above 2L models that were found to be favorable for the HER (Supporting Information Figure S8). For the 3L MoS_2 models, hydrogen can be adsorbed on the 2nd layer or 3rd layer (equivalent to 1st layer). Hence, 3L(2nd) and 3L(3rd) models were considered, and their calculated Gibbs free energies are shown in Figure 3e and 3f, respectively. The ΔG^0_H's of 3L(3rd) models were similar to those of the 2L models with either type of edge. Also, it was revealed that regardless of whether bonding occurs at the 2nd or 3rd layer, the S-edge

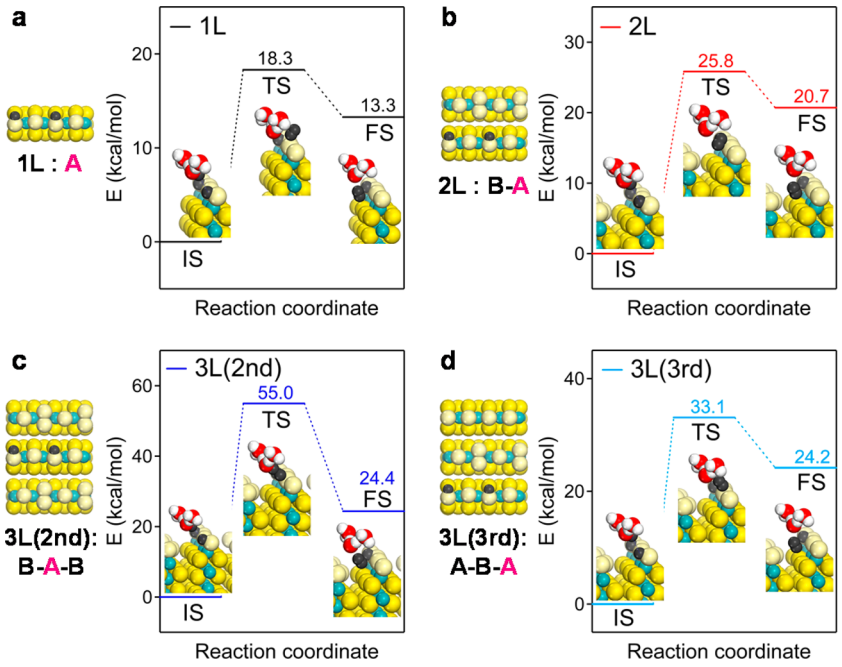

Figure 4. DFT calculations of the reaction paths on the Mo-edge layer models during the Heyrovsky reaction. The energy diagrams of the reaction paths on the Mo-edge (50% S) for a hydrogen coverage of 50% in the (a) 1L, (b) 2L, (c) 3L (2nd), and (d) 3L (3rd) models with respect to the reaction coordinate. The acronyms IS, TS, and FS represent the initial, transition, and final state, respectively. The numbers represent the relative energies of each state based on that of the IS. The black spheres represent either adsorbed H or desorbed H_2. The pink letter represents the layer with adsorbed H's.

produces a more thermo-neutral S−H bond (that is, close to a zero energy) than the Mo-edge. Comparing the two 3L models, the adsorption at the 2nd layer produces a more thermo-neutral S−H bond than the 3rd layer for the Mo-edge and a comparable thermo-neutral bond for the S-edge.

Calculations of Elementary Step Energetics for HER over MoS_2. From the aforementioned Gibbs free energy calculations, the energetically most favorable MoS_2 models (*i.e.*, Mo-edge(50% S) and S-edge(75% S)) for the HER could be deduced. Next, the energetics of elementary steps in the HER was calculated by tracking the reaction pathway in each MoS_2 model. As previous studies revealed, MoS_2 catalysts followed the Volmer-Heyrovsky mechanism during HER.[15,26,33,34] Heyrovsky reaction, which is the electrochemical desorption step, includes the combination of one adsorbed hydrogen atom and one proton freely floating in electrolyte. The latter proton must be introduced in water environments.[59,60] Thus, we modeled the solvated proton, which was originated from H_2SO_4, with two adjacent water molecules seizing the hydronium ion on both sides (*i.e.*, $H_3O^+(H_2O)_2$), and applied the implicit water environment by using the COSMO method.[61] With the simplified models, we investigated the energetics of the reaction paths for Heyrovsky reaction on Mo-edge first depending on the hydrogen coverage (Supporting Information Figure S10). We found that the heats of reaction and activation energies of 50% coverage of hydrogen were lower, thus more favorable than 25% coverage of hydrogen regardless of the layer numbers. Within the 50% coverage, separately adsorbed hydrogen atoms (denoted as "far" in Supporting Information Figure S10) are more favorable than closely adsorbed ones (denoted as "near" in Supporting Information Figure S10) since the former case shows smaller ΔG^0_H, thus more thermo-neutral (see Supporting Information Table S5). On the basis of the results, the most possible case for the HER of our interest was determined to be the 50% coverage of hydrogen, where two hydrogen atoms were separately adsorbed.

For further study on the effect of layer numbers on the HER, the energetics during the elementary reaction paths of two separately adsorbed hydrogen atoms at the Mo-edge in 1L (Model A), 2L (Model B-A), 3L(2nd) (Model B-A-B), and 3L(3rd) (Model A-B-A) models was calculated (Figure 4). As the number of layers was increased, the heat of reaction and activation energy at TS, where the adsorbed hydrogen atom combines with a proton in H_3O^+ at the edge site, were clearly increased because of the van der Waals (vdW) effect from adjacent S-edge layer(s). Similar activation energies of 2L and 3L(3rd) models revealed no significant influence of the top layer in the 3L(3rd) system. However, a clear difference in the activation energies between 3L(2nd) and 3L(3rd) models existed because of more vdW effects of adjacent S-edge layers located at both sides. In the case of the S-edge shown in Supporting Information Figure S11, the activation energy was increased as the number of layer was increased. Unlike the case of Mo-edge, both activation energies of 3L(2nd) and 3L(3rd) models were high since the S-edge top layer

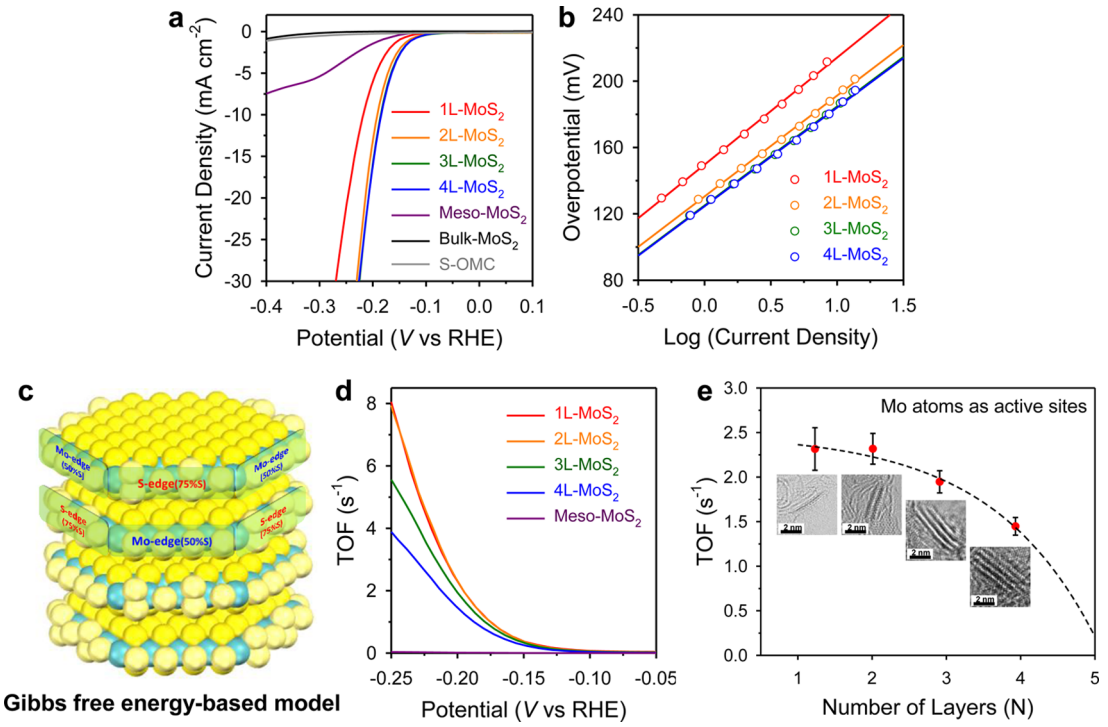

Figure 5. HER activity and TOF calculations. (a) Linear sweep voltammetry curves of the samples for the HER. (b) Tafel plots of LSV curves for MoS_2@OMC nanostructures. Linear portion of the plots were used to calculate the Tafel slopes. (c) MoS_2 structural model most suitable for the HER based on DFT calculations of the Gibbs free energy of hydrogen adsorption on MoS_2. (d and e) TOF calculations on MoS_2@OMC and Meso-MoS_2 nanostructures using the model shown in (c) and assuming Mo atoms at the Mo-edge as active sites: (d) TOFs with respect to potential and (e) TOFs at −200 mV (vs RHE) with respect to the number of layers (inset: Atomic resolution TEM images of corresponding MoS_2 nanoparticles in MoS_2@OMC nanostructures).

could exert the vdW effect on the adsorption S-edge layer at the bottom in the 3L(3rd) model. Even though increasing trend of the heat of reaction and activation energy was similar to the cases of Mo-edges, HER on S-edge of 1L model was not favored in comparison to that on Mo-edge due to larger heat of reaction and activation energy. Therefore, by evaluating the Mo- and S-edge cases, some important conclusions were drawn, which might be crucial for predicting HER activity: (i) the Mo-edge plays a major role in the HER, (ii) the S-edge can, in principle, be involved in HER in view of the thermo-neutral ΔG^0_H, yet little involved in view of Heyrovsky reaction, (iii) S-edge-type layers may severely hinder HER that occurs on the Mo-edge layer, and (iv) given the major role of the Mo-edge in HER with a little contributions from the S-edge, the best order for the HER might be 3L < 2L ≤ 1L.

HER Activity and Turnover Frequency of MoS_2@OMC Nanostructures. The preparation of MoS_2 nanoparticles with monolayer-precision allowed us to investigate particle size effects down to single layer level. We explored the electrocatalytic properties of MoS_2@OMC nanostructures in the HER (Figure 5). For comparison, the HER activities of bulk MoS_2, Meso-MoS_2, and sulfided OMC (S-OMC) were also measured. The details of the electrochemical measurements are described in Supporting Information. For all samples, the linear sweep voltammetry (LSV) curves were measured five times and the average data were used (Supporting Information Figure S12). For the MoS_2@OMC nanostructures, the LSV data were presented after the *iR* correction, for which series resistances were measured using electrochemical impedance spectroscopy (EIS) (Supporting Information Figure S13 and Table S6). As shown in Figure 5a, only a small amount of current was derived from the bulk MoS_2 and S-OMC even at high overpotential greater than 300 mV; such low catalytic activity could originate from the low intrinsic conductivity of bulk MoS_2 and the small number of active sites in S-OMC. In contrast, the MoS_2@OMC catalysts showed on-set potentials in the range of 120−132 mV with comparatively low overpotentials. In addition, the MoS_2@OMC catalysts exhibited a current density of -10 mA cm^{-2} in the overpotential range 178−192 mV (Supporting Information Table S7). Tafel slopes were extracted (Figure 5b) from the linear regression of the Tafel plots. The Tafel slopes of the MoS_2@OMC catalysts were between 60 and 65 mV/dec, which were similar to those of other metal sulfide catalysts, such as MoS_2 nanoparticles on Au surface (55−60 mV/dec),[13] amorphous molybdenum sulfide (60 mV/dec),[22] and $[Mo_3S_{13}]^{2-}$ clusters on highly oriented pyrolytic graphite (HOPG) (57 mV/dec).[35]

To gain a quantitative insight into the HER activity, the turnover frequency (TOF) of the MoS_2@OMC catalysts was calculated. While the overpotential of catalysts

has relevance to their device applicability, TOFs can reveal an intrinsic catalytic activity of single active site in MoS_2 nanoparticles. For the TOF calculations, MoS_2 structural model (Figure 5c), based on the Gibbs free energy calculation-optimized layers (Model A and B in Figure 3a), were constructed. With the MoS_2 model in Figure 5c and the observed size of MoS_2 nanoparticles in the MoS_2@OMC, the number of each type of atoms in the edge could be calculated (Supporting Information for details). Mo atoms at the Mo-edges were considered as active sites, similar to that in previous works.[9,13,35] Among the compared catalysts, the 1L- and 2L-MoS_2@OMC catalysts showed the highest activity, with a TOF of 2.32 s^{-1} at an overpotential of 200 mV (Figure 5d and Supporting Information Table S7). Comparison with the TOFs of previously reported MoS_2-based catalysts at the same overpotential (Figure 4d in ref 35) indicated the very high TOF of 1L- and 2L-MoS_2@OMCs, which approached the TOF of $[Mo_3S_{13}]^{2-}$ clusters on HOPG ($\sim$3 s^{-1}) reported by Bessenbacher and co-workers[35] and was higher than the TOFs of MoS_2 on reduced graphene oxide,[15] electrodeposited amorphous MoS_3,[21] and double gyroid structured MoS_2.[31] Upon examination of the HER activity trend of the MoS_2@OMC catalysts, it is clear that the TOF values nonlinearly decreased with increased layer numbers in MoS_2 nanoparticles (Figure 5e). While the HER activity was nearly preserved from 1L- to 2L-MoS_2@OMC, it rapidly diminished upon stacking additional MoS_2 layers. The more remarkable change of TOFs from 2L to 3L compared to that from 1L to 2L can be explained by the energetics of the HER. A similar trend is observed for the change of activation energy required to overcome the transition state in Figure 4. The activation energy increases more rapidly from 2L to 3L than from 1L to 2L, demonstrating that the activation energy is an important factor for determining the HER performance. The origin of the increasing trend in HER activity with decreased MoS_2 layer number was attributed to a combination of several factors, including the increased number of edge sulfur sites, their enhanced surface oxidation, and the evolution of the 1T phase, as confirmed by EXAFS and XPS analyses. In addition, the increase in activation energy at the transition state (TS in Figure 4) with layer numbers owing to the vdW effect could also play an important role in governing the HER activity.

We also carried out TOF calculations, assuming S atoms on the Mo-edges as the active sites, as the HER is initiated by the adsorption of H atoms on such unsaturated S atoms (Supporting Information Figure S14a,b). The HER activity trend over the MoS_2@OMC catalysts was similar to the aforementioned calculation, yet the TOF values for this case were higher. In addition, as the S-edges can also be involved in the HER, the TOFs of the MoS_2@OMC catalysts were also calculated, assuming that the S atoms in both the Mo- and S-edges were involved in the HER (Supporting Information Figure S14c,d). In addition, the TOF calculations were extended using the structural model deduced from the binding energy calculations (Supporting Information Figure S15a). With this model, the TOFs were calculated by assuming the active sites were (i) Mo atoms in the Mo-edge (Supporting Information Figure S15b,c), (ii) S atoms in the Mo-edge (Supporting Information Figure S15d,e), and (iii) S atoms in the Mo- and S-edge (Supporting Information Figure S15f,g). All TOF calculations consistently suggested decreasing HER activities in a quasi-linear manner with increasing layer numbers in the MoS_2.

Preparation and HER Activity of $CoMoS_2$@OMC Nanostructures. To generalize the nanopore-confined synthesis of metal sulfide nanoparticles and to confirm the HER activity trend, we prepared cobalt-doped MoS_2@OMC ($CoMoS_2$@OMC) nanostructures. Previously, it was shown that the addition of Co atoms in MoS_2 can boost the HER activity.[26] The characterization of the two $CoMoS_2$@OMC nanostructures by SEM, EDS elemental mapping, XRD, nitrogen adsorption (Supporting Information Figures S16–S19), and ICP-OES analysis (Supporting Information Table S1) clearly revealed the successful formation of mesoporous structures with large surface area and homogeneous distributions of the respective elements of the $CoMoS_2$ nanoparticles. TEM images of $CoMoS_2$@OMCs (Figure 6a,b) clearly showed that the $CoMoS_2$ nanoparticles were successfully embedded within the OMC arrays, like the MoS_2 nanoparticles within the MoS_2@OMC nanostructures. The combination of TEM images and layer number analysis (Supporting Information Figure S20 and Table S2) indicated that the two $CoMoS_2$@OMCs with different $CoMoS_2$ loading had an average of 2.5 and 3.5 layers (hereafter denoted as 2.5L-$CoMoS_2$@OMC and 3.5L-$CoMoS_2$@OMC, respectively). The Mo K-edge EXAFS fitting spectra of the $CoMoS_2$@OMC nanostructures (Supporting Information Figure S21a) exhibited very similar peak positions and intensities to those of MoS_2@OMCs. The Co K-edge EXAFS spectra (Supporting Information Figure S21b) revealed the absence of Co–Co and Co–Mo bonds, indicating that Co was atomically incorporated into the MoS_2 nanoparticles, and that most Co atoms were located on the edge sites rather than the basal plane, as suggested by Hu and co-workers.[26] The EXAFS results were further substantiated by Co 2p XPS analysis (Supporting Information Figure S22c), as signals arising from Co_9S_8 and CoMo alloys were not observed.[29] The Mo 3d and S 2p XPS spectra of $CoMoS_2$@OMC nanostructures (Supporting Information Figure S22b,d) showed similar trends with those of MoS_2@OMCs; the peaks corresponding to Mo^{5+}, Mo^{6+} and S_2^{2-} oxidation states became more noticeable with decreased $CoMoS_2$ layer numbers, indicating enhanced surface oxidation and an increased population of S_2^{2-} species.

The HER activity of $CoMoS_2$@OMC catalysts was investigated and revealed enhanced catalytic activity

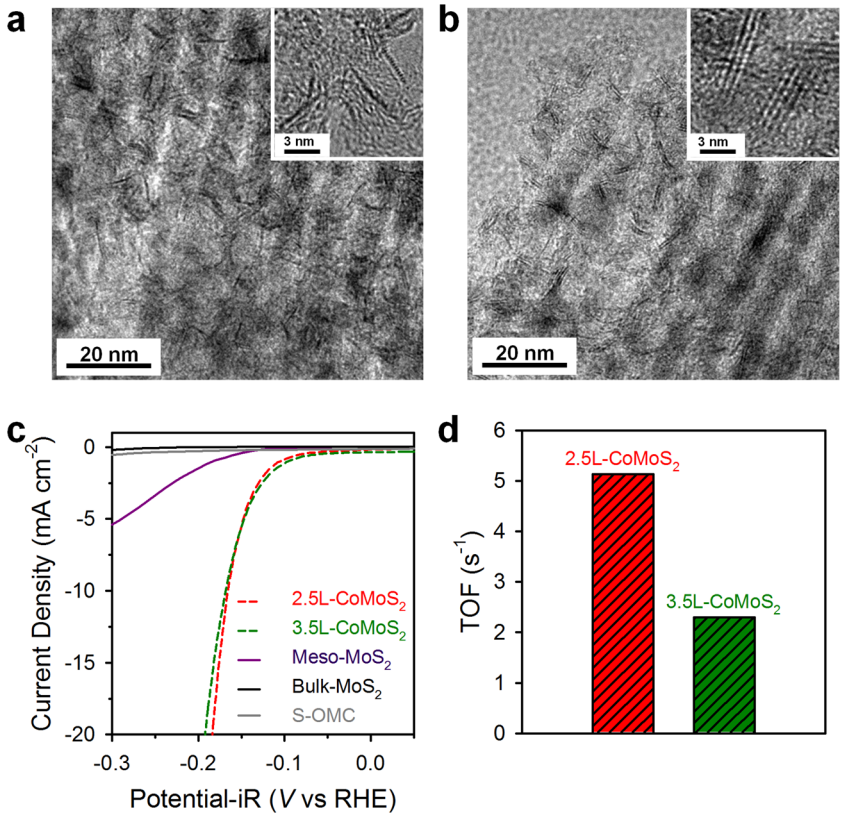

Figure 6. TEM characterization and HER activity of $CoMoS_2$@OMC. TEM images of (a) 2.5L- and (b) 3.5L-$CoMoS_2$@OMC nanostructures. Inset images in (a) and (b) are the corresponding HRTEM images. (c) Linear sweep voltammetry curves after *iR* correction of the $CoMoS_2$@OMCs for the HER. (d) TOFs of $CoMoS_2$@OMC at −200 mV (vs RHE).

as compared to undoped MoS_2@OMC catalysts; an overpotential of 166−170 mV at a current density of -10 mA cm^{-2} (Figure 6c and Supporting Information Table S7) was observed. The enhanced catalytic capability was corroborated by the EIS, as the Nyquist plots for the $CoMoS_2$@OMC catalysts exhibited substantially reduced charge transfer resistance as compared to those of MoS_2@OMC (Supporting Information Figure S23 and Table S6). The TOFs of $CoMoS_2$@OMC were calculated using the Gibbs free energy calculation-driven structural model (Figure 5c), by assuming the Mo edge atoms as active sites. The TOFs of 2.5L- and 3.5L-$CoMoS_2$@OMC catalysts were 5.13 and 2.30 s^{-1}, respectively, which was higher than that of MoS_2@OMC, confirming the promotion effect of the Co dopant. The enhanced HER activity of $CoMoS_2$@OMC catalysts was attributed to the involvement of the S-edges in the HER.[12,26] Significantly, $CoMoS_2$@OMC showed a similar trend of increasing HER activity with decreasing $CoMoS_2$ layer number, as in the case of the MoS_2@OMC catalysts (Figure 6d and Supporting Information Table S7). Finally, the durability of the 3.5L-$CoMoS_2$@OMC catalyst, which showed the best activity, was assessed by measuring the HER activity after cycling the potential between −0.3 and 0.1 V 1000 times. The LSV of 3.5L-$CoMoS_2$@OMC after cycling showed only a very small negative shift in the potential (Supporting Information Figure S24), indicating the stability of the catalysts upon prolonged operation.

CONCLUSIONS

We have demonstrated the preparation of MoS_2 nanoparticles with discrete layer numbers *via* nanopore-confined synthesis, which enabled the investigation of nanoscale size effects in the HER. The most favorable single-, double-, and triple-layer MoS_2 model structures for the HER were deduced using DFT calculations; with these models, the detailed energetics of elementary reactions during the HER was calculated. By combining the HER activity measurements with the DFT calculation results, we established that the TOFs of MoS_2@OMC for the HER clearly decreased in a quasi-linear manner with an increase in the layer number of MoS_2 nanoparticles. The enhanced activity in smaller MoS_2 nanoparticles was attributed to a combination of several factors, including the high ratio of edge sulfur sites, tendency toward enhanced surface oxidation, propensity toward 1T phase formation, and lower activation energy required to overcome the transition state. Even though it was not considered in this work, electron hopping efficiency between layers has recently been suggested as being another important factor influencing the HER performance.[62] The HER activity trend observed with MoS_2@OMC was generalized

with $CoMoS_2$@OMC nanostructures. The nanopore-confined synthesis strategy that combined controllability with monolayer-precision and suitability for large-scale synthesis can be generalized to other metal chalcogenides. We believe that the improvement of synthetic procedure would yield MoS_2 nanoparticles with more narrow size distribution, which in turn can be used as more reliable platform for investigating the nanoscale size effect. In addition, to interrogate the origin of HER activity in our catalysts, the behavior of active species during HER will be investigated by using *in situ* electrochemical X-ray absorption methods combined with theoretical calculations. Finally, the discernments gleaned from this work can provide crucial information for designing advanced HER catalysts, and may also be applied to other metal sulfide-catalyzed reactions such as hydrodesulfurization.[63]

MATERIALS AND METHODS

Synthesis of MS_2@OMC (M = Mo and CoMo). The general synthetic procedure for MS_2@OMC (M-Mo and CoMo) nanostructures consists of (i) partial filling of mesopores of SBA-15 silica template with carbon structure, (ii) subsequent formation of metal sulfide nanostructures inside the void spaces of carbon-SBA-15 composites, and (iii) etching of the SBA-15 template. The preparation of MoS_2@OMC is described as follows: 6.10 g of sucrose (Samchun) was dissolved in 20 g of DI water in a PP bottle, and 0.69 g of H_2SO_4 (95%, Samchun) was added to the solution. Then, 4.0 g of SBA-15 was added to the sucrose solution, and the mixture was gently agitated to make a homogeneous paste. This paste was heated to 100 °C and maintained at this temperature for 6 h, then was subsequently kept at 160 °C for 2 h under air. The brownish product was then carbonized at 400 °C for 4 h, and at 900 °C for 2 h under N_2 gas at a flow rate of 1 L min^{-1}. To the resulting carbon-SBA-15 composite, the molybdenum precursor was impregnated and sulfided to generate MoS_2-carbon-silica composites. A specific amount (0.056, 0.11, 0.22, 0.45, 0.66, or 1.11 g) of phosphomolybdic acid hydrate (PMA, Sigma-Aldrich) was dissolved in 5 g of absolute ethanol, and 1.15 g of the as-synthesized carbon-SBA-15 composite was added to the solution. The mixture was stirred at 35 °C to evaporate the solvent, and finely ground in an agate mortar. The resulting powder was sulfided by raising the temperature to 600 °C at a heating rate of 2 °C min^{-1} and maintained at 600 °C for 5 h under 10% H_2S (balanced with Ar) gas at a flow rate of 200 mL min^{-1}. After sulfidation, the furnace was cooled to room temperature (RT) under N_2 gas flow. Finally, the SBA-15 silica template was etched with HF. The nominal loadings of MoS_2, based on the quantities of PMA precursor listed above, were 5, 10, 15, and 20 wt %. The synthesis of cobalt-doped $CoMoS_2$@OMC nanostructures was carried out in the same manner as MoS_2@OMC, but with a mixture of cobalt and molybdenum precursors. Specified amounts of cobalt(II) nitrate hexahydrate ($Co(NO_3)_2 \cdot 6H_2O$, Sigma-Aldrich) and PMA at a fixed molar ratio of Co:Mo = 1:3 were used.

Model Systems for Calculations. It is well-known that a MoS_2 layer contains two types of edges: Mo-edge ($10\bar{1}0$) and S-edge ($\bar{1}010$), and the ratio of the two edge types should be one-to-one in a stable layer.[58] For this structure, the reactivity of the layer varies by different sulfur coverage. When the layers are stacked, many combinatorial sets should be considered. We have systematically chosen model systems, based on the representative edges of Mo and S, which exhibit stable adsorption and efficient HER. The model systems were generated based on single-, double-, and triple-layer structures (1L, 2L, and 3L, respectively) of MoS_2. For 1L, the coverage of unsaturated sulfur atoms attached at the Mo-edge was 0, 50, and 100%, and that of the S-edge was 50, 75, and 100%. From the calculations of the 1L MoS_2 model, the Mo-edge (0% S coverage) and S-edge (50% S) were not further considered in the calculations involving the 2L or 3L models, due to the instability of both of these structures,[58] especially the instability of the latter when hydrogen is adsorbed. Hence, for 2L models, a total of eight systems were constructed, based on the combinatorial sets of Mo-edge (50% and 100% S) and S-edge (75% and 100% S). For 3L models, accounting for the two types by stacking order (Mo−S−Mo and S−Mo−S edges), we have constructed total of 12 systems. In each system, the locations for the adsorption of hydrogen are the Mo-edge (50% S) or S-edge (75% S) layer, which are predicted to be favorable for HER. Supporting Information Figure S8 displays all the systems considered for 1L, 2L, and 3L models. Note that A, A′, B, and B′ represent Mo-edge(50% and 100% S) and S-edge(75% and 100% S), respectively. It is worth noting that we have used a more stable form of S-edge(100% S), which shows a zigzag structure of two S_2 dimers (see Figure S9 in Supporting Information). This structure is more stable by ~0.1 eV than the structure of two S_2 dimers presented in other studies.[56,57]

Conflict of Interest: The authors declare no competing financial interest.

Acknowledgment. This work was supported by the Basic Science Research Program through the National Research Foundation (NRF) of Korea (NRF-2013R1A1A2012960 to S.H.J. and NRF-2013R1A1A2007491 to S.K.K.), the New & Renewable Energy Core Technology Program of the KETEP funded by the Ministry of Trade, Industry & Energy (MOTIE, 20133030011320), Korea Evaluation Institute of Industrial Technology by the MOTIE (10050509), and the Korea CCS R&D Center (KCRC) grant funded by the Ministry of Science, ICT & Future Planning (NRF-2013MiA8A1039968). B.S. and Y.J.S. acknowledge the Global Ph. D. Fellowship (NRF-2013H1A2A1032647 to B.S. and NRF-2013H1A2A1032644 to Y.J.S.). J.Y.C. acknowledges the National Junior Research Fellowship (NRF-2013H1A8A1003741). The EXAFS experiments performed at Pohang Light Source (PLS) were supported in part by the Ministry of Education and POSTECH.

Supporting Information Available: experimental and calculation sections, Tables S1−7, Figures S1−24, and related references. This material is available free of charge *via* the Internet at http://pubs.acs.org.

REFERENCES AND NOTES

1. Tenne, R. Inorganic Nanotubes and Fullerene-Like Nanoparticles. *Nat. Nanotechnol.* **2006**, *1*, 103–111.
2. Geim, A. K.; Grigorieva, I. V. van der Waals Heterostructures. *Nature* **2013**, *499*, 419–425.
3. Nicolosi, V.; Chhowalla, M.; Kanatzidis, M. G.; Strano, M. S.; Coleman, J. N. Liquid Exfoliation of Layered Materials. *Science* **2013**, *340*, 1420–1438.
4. Chhowalla, M.; Shin, H. S.; Eda, G.; Li, L.-J.; Loh, K. P.; Zhang, H. The Chemistry of Two-Dimensional Layered Transition Metal Dichalcogenide Nanosheets. *Nat. Chem.* **2013**, *5*, 263–275.
5. Butler, S. Z.; Hollen, S. M.; Cao, L.; Cui, Y.; Gupta, J. A.; Gutiérrez, H. R.; Heinz, T. F.; Hong, S. S.; Huang, J.; Ismach, A. F.; et al. Progress, Challenges, and Opportunities in Two-Dimensional Materials Beyond Graphene. *ACS Nano* **2013**, *7*, 2898–2926.
6. Merki, D.; Hu, X. Recent Developments of Molybdenum and Tungsten Sulfides as Hydrogen Evolution Catalysts. *Energy Environ. Sci.* **2011**, *4*, 3878–3888.
7. Laursen, A. B.; Kegnæs, S.; Dahl, S.; Chorkendorff, I. Molybdenum Sulfides—Efficient and Viable Materials for Electro- and Photoelectrocatalytic Hydrogen Evolution. *Energy Environ. Sci.* **2012**, *5*, 5577–5591.

8. Yan, Y.; Xia, B.; Xu, Z.; Wang, X. Recent Development of Molybdenum Sulfides as Advanced Electrocatalysts for Hydrogen Evolution Reaction. *ACS Catal.* **2014**, *4*, 1693–1705.
9. Morales-Guio, C. G.; Hu, X. Amorphous Molybdenum Sulfides as Hydrogen Evolution Catalysts. *Acc. Chem. Res.* **2014**, *47*, 2671–2681.
10. Yang, J.; Shin, H. S. Recent Advances in Layered Transition Metal Dichalcogenides for Hydrogen Evolution Reaction. *J. Mater. Chem. A* **2014**, *2*, 5979–5985.
11. Hinnemann, B.; Moses, P. G.; Bonde, J.; Jørgensen, K. P.; Nielsen, J. H.; Horch, S.; Chorkendorff, I.; Nørskov, J. K. Biomimetic Hydrogen Evolution: MoS_2 Nanoparticles as Catalyst for Hydrogen Evolution. *J. Am. Chem. Soc.* **2005**, *127*, 5308–5309.
12. Bonde, J.; Moses, P. G.; Jaramillo, T. F.; Nørskov, J. K.; Chorkendorff, I. Hydrogen Evolution on Nano-Particulate Transition Metal Sulphides. *Faraday Discuss.* **2008**, *140*, 219–231.
13. Jaramillo, T. F.; Jørgensen, K. P.; Bonde, J.; Nielsen, J. H.; Horch, S.; Chorkendorff, I. Identification of Active Edge Sites for Electrochemical H_2 Evolution from MoS_2 Nanocatalysts. *Science* **2007**, *317*, 100–102.
14. Karunadasa, H. I.; Montalvo, E.; Sun, Y.; Majda, M.; Long, J. R.; Chang, C. J. Molecular MoS_2 Edge Site Mimic for Catalytic Hydrogen Generation. *Science* **2012**, *335*, 698–702.
15. Li, Y.; Wang, H.; Xie, L.; Liang, Y.; Hong, G.; Dai, H. MoS_2 Nanoparticles Grown on Graphene: An Advanced Catalyst for the Hydrogen Evolution Reaction. *J. Am. Chem. Soc.* **2011**, *133*, 7296–7299.
16. Firmiano, E. G. S.; Cordeiro, M. A. L.; Rabelo, A. C.; Dalmaschio, C. J.; Pinheiro, A. N.; Pereira, E. C.; Leite, E. R. Graphene Oxide as a Highly Selective Substrate to Synthesize a Layered MoS_2 Hybrid Electrocatalyst. *Chem. Commun.* **2012**, *48*, 7687–7689.
17. Laursen, A. B.; Vesborg, P. C. K.; Chorkendorff, I. A High-Porosity Carbon Molybdenum Sulphide Composite with Enhanced Electrochemical Hydrogen Evolution and Stability. *Chem. Commun.* **2013**, *49*, 4965–4967.
18. Chang, Y.-H.; Lin, C.-T.; Chen, T.-Y.; Hsu, C.-L.; Lee, Y.-H.; Zhang, W.; Wei, K.-H.; Li, L.-J. Highly Efficient Electrocatalytic Hydrogen Production by MoS_x Grown on Graphene-Protected 3D Ni Foams. *Adv. Mater.* **2013**, *25*, 756–760.
19. Yan, Y.; Ge, X.; Liu, Z.; Wang, J.-Y.; Lee, J.-M.; Wang, X. Facile Synthesis of Low Crystalline MoS_2 Nanosheet-Coated CNTs for Enhanced Hydrogen Evolution Reaction. *Nanoscale* **2013**, *5*, 7768–7771.
20. Liao, L.; Zhu, J.; Bian, X.; Zhu, L.; Scanlon, M. D.; Girault, H. H.; Liu, B. MoS_2 Formed on Mesoporous Graphene as a Highly Active Catalyst for Hydrogen Evolution. *Adv. Funct. Mater.* **2013**, *23*, 5326–5333.
21. Merki, D.; Fierro, S.; Vrubel, H.; Hu, X. Amorphous Molybdenum Sulfide Films as Catalysts for Electrochemical Hydrogen Production in Water. *Chem. Sci.* **2011**, *2*, 1262–1267.
22. Benck, J. D.; Chen, Z.; Kuritzky, L. Y.; Forman, A. J.; Jaramillo, T. F. Amorphous Molybdenum Sulfide Catalysts for Electrochemical Hydrogen Production: Insights into the Origin of their Catalytic Activity. *ACS Catal.* **2012**, *2*, 1916–1923.
23. Vrubel, H.; Merki, D.; Hu, X. Hydrogen Evolution Catalyzed by MoS_3 and MoS_2 Particles. *Energy Environ. Sci.* **2012**, *5*, 6136–6144.
24. Vrubel, H.; Hu, X. Growth and Activation of an Amorphous Molybdenum Sulfide Hydrogen Evolving Catalyst. *ACS Catal.* **2013**, *3*, 2002–2011.
25. Lu, Z.; Zhang, H.; Zhu, W.; Yu, X.; Kuang, Y.; Chang, Z.; Lei, X.; Sun, X. *In Situ* Fabrication of Porous MoS_2 Thin-Films as High-Performance Catalysts for Electrochemical Hydrogen Evolution. *Chem. Commun.* **2013**, *49*, 7516.
26. Merki, D.; Vrubel, H.; Rovelli, L.; Fierro, S.; Hu, X. Fe, Co, and Ni ions Promote the Catalytic Activity of Amorphous Molybdenum Sulfide Films for Hydrogen Evolution. *Chem. Sci.* **2012**, *3*, 2515–2525.
27. Tran, P. D.; Nguyen, M.; Pramana, S. S.; Bhattacharjee, A.; Chiam, S. Y.; Fize, J.; Field, M. J.; Artero, V.; Wong, L. H.; Loo, J.; et al. Copper Molybdenum Sulfide: A New Efficient Electrocatalyst for Hydrogen Production from Water. *Energy Environ. Sci.* **2012**, *5*, 8912–8916.
28. Kim, J.; Byun, S.; Smith, A. J.; Yu, J.; Huang, J. Enhanced Electrocatalytic Properties of Transition-Metal Dichalcogenides Sheets by Spontaneous Gold Nanoparticle Decoration. *J. Phys. Chem. Lett.* **2013**, *4*, 1227–1232.
29. Tran, P. D.; Chiam, S. Y.; Boix, P. P.; Ren, Y.; Pramana, S. S.; Fize, J.; Artero, V.; Barber, J. Novel Cobalt/Nickel–Tungsten-Sulfide Catalysts for Electrocatalytic Hydrogen Generation from Water. *Energy Environ. Sci.* **2013**, *6*, 2452–2459.
30. Sun, X.; Dai, J.; Guo, Y.; Wu, C.; Hu, F.; Zhao, J.; Zeng, X.; Xie, Y. Semimetallic Molybdenum Disulfide Ultrathin Nanosheets as an Efficient Electrocatalyst for Hydrogen Evolution. *Nanoscale* **2014**, *6*, 8359–8367.
31. Kibsgaard, J.; Chen, Z.; Reinecke, B. N.; Jaramillo, T. F. Engineering the Surface Structure of MoS_2 to Preferentially Expose Active Edge Sites for Electrocatalysis. *Nat. Mater.* **2012**, *11*, 963–969.
32. Wu, Z.; Fang, B.; Wang, Z.; Wang, C.; Liu, Z.; Liu, F.; Wang, W.; Alfantazi, A.; Wang, D.; Wilkinson, D. P. MoS_2 Nanosheets: A Designed Structure with High Active Site Density for the Hydrogen Evolution Reaction. *ACS Catal.* **2013**, *3*, 2101–2107.
33. Xie, J.; Zhang, H.; Li, S.; Wang, R.; Sun, X.; Zhou, M.; Zhou, J.; Lou, X. W.; Xie, Y. Defect-Rich MoS_2 Ultrathin Nanosheets with Additional Active Edge Sites for Enhanced Electrocatalytic Hydrogen Evolution. *Adv. Mater.* **2013**, *25*, 5807–5813.
34. Xie, J.; Zhang, J.; Li, S.; Grote, F.; Zhang, X.; Zhang, H.; Wang, R.; Lei, Y.; Pan, B.; Xie, Y. Controllable Disorder Engineering in Oxygen-Incorporated MoS_2 Ultrathin Nanosheets for Efficient Hydrogen Evolution. *J. Am. Chem. Soc.* **2013**, *135*, 17881–17888.
35. Kibsgaard, J.; Jaramillo, T. F.; Besenbacher, F. Building an Appropriate Active-Site Motif into a Hydrogen-Evolution Catalyst with Thiomolybdate $[Mo_3S_{13}]^{2-}$ Clusters. *Nat. Chem.* **2014**, *6*, 248–253.
36. Chung, D. Y.; Park, S.-K.; Chung, Y.-H.; Yu, S.-H.; Lim, D.-H.; Jung, N.; Ham, H. C.; Park, H.-Y.; Piao, Y.; Yoo, S. J.; et al. Edge-Exposed MoS_2 Nano-Assembled Structures as Efficient Electrocatalysts for Hydrogen Evolution Reaction. *Nanoscale* **2014**, *6*, 2131–2136.
37. Lukowski, M. A.; Daniel, A. S.; Meng, F.; Forticaux, A.; Li, L.; Jin, S. Enhanced Hydrogen Evolution Catalysis from Chemically Exfoliated Metallic MoS_2 Nanosheets. *J. Am. Chem. Soc.* **2013**, *135*, 10274–10277.
38. Voiry, D.; Yamaguchi, H.; Li, J.; Silva, R.; Alves, D. C. B.; Fujita, T.; Chen, M.; Asefa, T.; Shenoy, V. B.; Eda, G.; et al. Enhanced Catalytic Activity in Strained Chemically Exfoliated WS_2 Nanosheets for Hydrogen Evolution. *Nat. Mater.* **2013**, *12*, 850–855.
39. Voiry, D.; Salehi, M.; Silva, R.; Fujita, T.; Chen, M.; Asefa, T.; Shenoy, V. B.; Eda, G.; Chhowalla, M. Conducting MoS_2 Nanosheets as Catalysts for Hydrogen Evolution Reaction. *Nano Lett.* **2013**, *13*, 6222–6227.
40. Wang, H.; Lu, Z.; Xu, S.; Kong, D.; Cha, J. J.; Zheng, G.; Hsu, P.-C.; Yan, K.; Bradshaw, D.; Prinz, F. B.; et al. Electrochemical Tuning of Vertically Aligned MoS_2 Nanofilms and Its Application in Improving Hydrogen Evolution Reaction. *Proc. Natl. Acad. Sci. U.S.A.* **2013**, *110*, 19701–19706.
41. Boudart, M. Catalysis by Supported Metals. *Adv. Catal.* **1969**, *20*, 153–166.
42. Van Santen, R. A. Complementary Structure Sensitive and Insensitive Catalytic Relationships. *Acc. Chem. Res.* **2009**, *42*, 57–66.
43. Koper, M. T. M. Structure Sensitivity and Nanoscale Effects in Electrocatalysis. *Nanoscale* **2011**, *3*, 2054–2073.
44. Chen, M. S.; Goodman, D. W. The Structure of Catalytically Active Gold on Titania. *Science* **2004**, *306*, 252–255.
45. Kaden, W. E.; Wu, T.; Kunkel, W. A.; Anderson, S. L. Electronic Structure Controls Reactivity of Size-Selected Pd Clusters Adsorbed on TiO_2 Surfaces. *Science* **2009**, *326*, 826–829.

46. Joo, S. H.; Park, J. Y.; Renzas, J. R.; Butcher, D. R.; Huang, W.; Somorjai, G. A. Size Effect of Ruthenium Nanoparticles in Catalytic Carbon Monoxide Oxidation. *Nano Lett.* **2010**, *10*, 2709–2713.
47. Yamamoto, K.; Imaoka, T.; Chun, W.-J.; Enoki, O.; Katoh, H.; Takenaga, M.; Sonoi, A. Size-Specific Catalytic Activity of Platinum Clusters Enhances Oxygen Reduction Reactions. *Nat. Chem.* **2009**, *1*, 397–402.
48. Nesselberger, M.; Ashton, S.; Meier, J. C.; Katsounaros, I.; Mayrhofer, K. J. J.; Arenz, M. The Particle Size Effect on the Oxygen Reduction Reaction Activity of Pt Catalysts: Influence of Electrolyte and Relation to Single Crystal Models. *J. Am. Chem. Soc.* **2011**, *133*, 17428–17433.
49. Jun, S.; Joo, S. H.; Ryoo, R.; Kruk, M.; Jaroniec, M.; Liu, Z.; Ohsuna, T.; Terasaki, O. Synthesis of New, Nanoporous Carbon with Hexagonally Ordered Mesostructure. *J. Am. Chem. Soc.* **2000**, *122*, 10712–10713.
50. Shi, Y.; Wan, Y.; Liu, R.; Tu, B.; Zhao, D. Synthesis of Highly Ordered Mesoporous Crystalline WS_2 and MoS_2 *via* a High-Temperature Reductive Sulfuration Route. *J. Am. Chem. Soc.* **2007**, *129*, 9522–9531.
51. Liu, H.; Su, D.; Zhou, R.; Sun, B.; Wang, G.; Qiao, S. Z. Highly Ordered Mesoporous MoS_2 with Expanded Spacing of the (002) Crystal Plane for Ultrafast Lithium Ion Storage. *Adv. Energy Mater.* **2012**, *2*, 970–975.
52. Chen, Z.; Cummins, D.; Reinecke, B. N.; Clark, E.; Sunkara, M. K.; Jaramillo, T. F. Core-Shell MoO_3-MoS_2 Nanowires for Hydrogen Evolution: A Functional Design for Electrocatalytic Materials. *Nano Lett.* **2011**, *11*, 4168–4175.
53. Yan, Y.; Xia, B.; Ge, X.; Liu, Z.; Wang, J.-Y.; Wang, X. Ultrathin MoS_2 Nanoplates with Rich Active Sites as Highly Efficient Catalyst for Hydrogen Evolution. *ACS Appl. Mater. Interfaces* **2013**, *5*, 12794–12798.
54. Tsai, C.; Abild-Pedersen, F.; Nørskov, J. K. Tuning the MoS_2 Edge-Site Activity for Hydrogen Evolution *via* Support Interactions. *Nano Lett.* **2014**, *14*, 1381–1387.
55. Bollinger, M. V.; Jacobsen, K. W.; Nørskov, J. K. Atomic and Electronic Structure of MoS_2 Nanoparticles. *Phys. Rev. B* **2003**, *67*, 085410.
56. Hinnemann, B.; Nørskov, J. K.; Topsoe, H. A Density Functional Study of the Chemical Differences between Type I and Type II MoS_2-Based Structures in Hydrotreating Catalysts. *J. Phys. Chem. B* **2005**, *109*, 2245–2253.
57. Prodhomme, P. Y.; Raybaud, P.; Toulhoat, H. Free-Energy Profiles Along Reduction Pathways of MoS_2 M-Edge and S-Edge by Dihydrogen: A First-Principles Study. *J. Catal.* **2011**, *280*, 178–195.
58. Raybaud, P.; Hafner, J.; Kresse, G.; Kasztelan, S.; Toulhoat, H. Ab Initio Study of the H_2-H_2S/MoS_2 Gas-Solid Interface: The Nature of the Catalytically Active Sites. *J. Catal.* **2000**, *189*, 129–146.
59. Skulason, E.; Karlberg, G. S.; Rossmeisl, J.; Bligaard, T.; Greeley, J.; Jonsson, H.; Nørskov, J. K. Density Functional Theory Calculations for the Hydrogen Evolution Reaction in an Electrochemical Double Layer on the Pt(111) Electrode. *Phys. Chem. Chem. Phys.* **2007**, *9*, 3241–3250.
60. Wei, G. F.; Fang, Y. H.; Liu, Z. P. First Principles Tafel Kinetics for Resolving Key Parameters in Optimizing Oxygen Electrocatalytic Reduction Catalyst. *J. Phys. Chem. C* **2012**, *116*, 12696–12705.
61. Klamt, A.; Schuurmann, G. COSMO: A New Approach to Dielectric Screening in Solvents with Explicit Expressions for the Screening Energy and its Gradient. *J. Chem. Soc., Perkin Trans. 2* **1993**, 799–805.
62. Yu, Y.; Huang, S.-Y.; Li, Y.; Steinmann, S. N.; Yang, W.; Cao, L. Layer-Dependent Electrocatalysis of MoS_2 for Hydrogen Evolution. *Nano Lett.* **2014**, *14*, 553–558.
63. Lauritsen, J. V.; Nyberg, M.; Nørskov, J. K.; Clausen, B. S.; Topsøe, H.; Lægsgaard, E.; Besenbacher, F. Hydrodesulfurization Reaction Pathways on MoS_2 Nanoclusters Revealed by Scanning Tunneling Microscopy. *J. Catal.* **2004**, *224*, 94–106.